Front. Archit. Civ. Eng. China 2010, 4(2): 208–222
DOI 10.1007/s11709-010-0025-2

RESEARCH ARTICLE

Mingjing JIANG, Hehua ZHU, Xiumei LI

Strain localization analyses of idealized sands in biaxial tests by distinct element method

Abstract This paper presents a numerical investigation on the strain localization of an idealized sand in biaxial compression tests using the distinct element method (DEM). In addition to the dilatancy and material frictional angle, the principal stress field, and distributions of void ratio, particle velocity, and the averaged pure rotation rate (APR) in the DEM specimen are examined to illustrate the link between microscopic and macroscopic variables in the case of strain localization. The study shows that strain localization of the granular material in the tests proceeds with localizations of void ratio, strain and APR, and distortions of stress field and force chains. In addition, both thickness and inclination of the shear band change with the increasing of axial strain, with the former valued around 10–14 times of mean grain diameter and the later overall described by the Mohr-Coulomb theory.

Keywords idealized sand, strain localization, numerical analyses, distinct element method (DEM)

1 Introduction

Progressive failure analysis of geomaterials is considered as one of main parts in modern soil mechanics, because it is essentially associated with instability of embankments, slopes, dams, and excavations in geotechnical engineering [1]. It is well accepted in the geotechnical engineering community that strain localization (shear band) analysis is a precursor to solve this important problem [2,3]. In the past decades, lots of theoretical, experimental, and numerical works have been carried out on strain localization, particularly in granulates [4–7], although few works can be found on strain localization analysis of clays due to the theoretical, numerical, and technical difficulties in the study [8–12].

Strain localization theories are usually employed to predict the occurrence of shear band in geomaterials. In the analyses, shear band is regarded as a thin layer of material 'sandwiched' by two planes moving at inconsistent strain rates, and the formation of shear band is treated as a bifurcation point of homogeneous deformation. Hence, the condition for formation of shear band becomes mathematically equivalent to the occurrence of non-unique solution to the equilibrium equations for the geomaterial of a given constitutive laws in its initial configuration. Theoretical analyses show that in elasto-plastic materials, ellipticity of the equation of motion in a one-dimensional context is typically a result of loss of hyperbolicity, which signals instability and ill posedness. In the multidimensional context, strain localization and ill posedness have been considered as symptoms of material instability [13], and for non-associative plastic flow rules, the squares of two wave speeds might become complex conjugate. The theories have been successfully applied to traditional elasto-plastic materials without microstructure, which leads to zero thickness of shear band [4,5,14–18], and to Cosserat continuum in which the thickness of shear band is taken into account [19–21]. Nevertheless, the method has the following four limitations: 1) it is applicable only to the simple boundary-value problems, e.g., biaxial compression test, instead of complex problems; 2) it is able to predict the occurrence of shear band but unable to describe the subsequent deformation process; 3) it is unable to give a prediction of proper thickness and inclination of shear band [1]. This constitutes one strong motivation in this study.

Many experiments have been carried out on sands with efforts to clarify the relationships between the strain-softening behavior of sand and the formation of shear band, the experimental conditions, and the occurrence and inclination of shear band [22–27]. Advanced technologies, such as X-ray [28,29], the stereophoto-grammetric

Received December 9, 2009; accepted January 3, 2010

Mingjing JIANG (✉), Hehua ZHU, Xiumei LI
Department of Geotechnical Engineering and Key Laboratory of Geotechnical and Underground Engineering of Ministry of Education, Tongji University, Shanghai 200092, China
E-mail: mingjing.jiang@tongji.edu.cn

technique [30], or particle image velocimetry [31], have also been employed to investigate the strain field within or outside shear bands, their thickness and inclination, etc. The experimental observation demonstrates that shear bands are formed progressively in laboratory, from the invisible to the visible state with the naked eye. Generally, several parallel mini-bands are formed at first, then turn into several conjugate small shear bands, and finally into an obvious shear band in the specimen. However, these advanced technologies are still unable to provide some other important information about shear bands, such as particle rotations and contact force chains. This constitutes another strong motivation in this study.

Numerical analyses have been carried out on strain localization of sands by lots of researchers mostly using the finite element method (FEM). Most of the FEM analyses employ one the following types of methods: 1) special variables, such as fracture or damage variable [32,33] and criteria on occurrence and inclination of shear bands [34,35], are incorporated into constitutive models in FEM by which the bifurcation theory will be employed in the analyses. 2) Non-linear and rate-independent stress-strain relationships and displacement-type FEM are used in the analyses [36–39], in which the strain-softening behavior of sands usually needs to be included in the constitutive models [40]. 3) Non-local constitutive models [41–43], gradient-dependent constitutive models [44], or Cosserat continuum theory [19–21, 45–50] are employed in FEM analyses so that the microstructure of soils and their inherent internal length can be taken into account. Nevertheless, none of the methods has received universal acceptance in strain localization analyses yet [1]. For example, it is still impossible for method 3) to measure the model parameter associated with the material internal length in laboratory, while method 2) suffers from several defects, such as mesh-dependency [1].

An effective method to investigate the strain localization and the associated micro mechanisms for sands is the distinct element method (DEM) first proposed by Cundall et al. [51]. Unlike FEM that deals with soils as continuum, DEM treats soils as an assembly of discrete materials, starts with basic constitutive laws at interparticle contacts, and provides macroscopic/microscopic responses of the assembly under complex loading. DEM has been already employed to examine several aspects of soil mechanics successfully, including basic mechanical behavior of granulates [52–56], the failure criteria of granular materials in three-dimensional stress space [57], kinematic theories for granular flow [58], creep theory [59], the generalized effective stress and strength functions for unsaturated soils [60], yielding mechanism of microstructured soils at both macroscopic and microscopic levels [61–67], penetration mechanism in granular soils [68,69], and future constitutive models for penetration analyses [70]. It can also be used to verify couple-stress continuum [71]. Moreover, it has been employed to carry out strain localization analyses of granular materials in biaxial tests [72–75].

The main objective of this paper is to present an insight into the strain localization of idealized sands by DEM analysis. In contrast to the previous study in Refs. [72–75], the main feature of the study is that in addition to the dilatancy and material frictional angle, the principal stress field, and distributions of void ratio, particle velocity and the averaged pure rotation rate (APR) [76,77] are all examined within and outside shear bands to understand the link between microscopic and macroscopic responses during strain localization. In addition, both the thickness and inclination of shear bands are analyzed at different stages of strain localization. Note that compression is taken as positive in describing stress or strain tensor in this paper.

2 DEM numerical tests

The contact model employed in the study, which controls the mechanical behavior of a contact between two particles, is a standard model originally proposed by Cundall et al. [51,78]. Figure 1 presents the main features of the model in physics. The model is physically made by a combination of a spring, a dash-pot, and a divider in both the normal and tangential direction, plus a slider in the tangential direction. Therefore, the model parameters are K_n the normal contact stiffness, K_s the tangential contact stiffness, and the interparticle coefficient of friction.

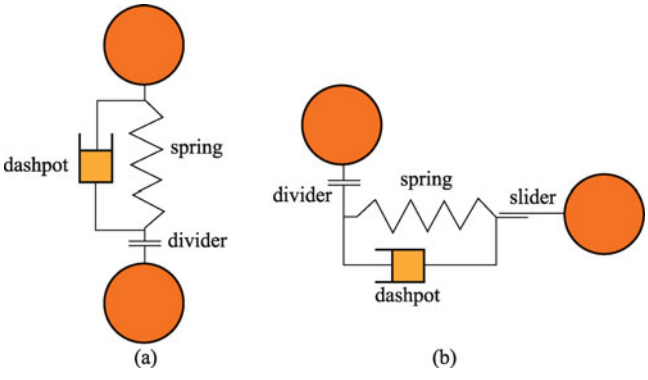

Fig. 1 Contact model for the idealized sands in DEM analyses. (a) Normal direction; (b) tangential direction

Figure 2 provides the particle size distribution, and Table 1 presents sample size and material parameters used in the DEM analyses. Ten different radii of particles have been used with the mean particle diameter d_{50} being 7.6 mm and the uniformity coefficient C_u 1.3. These ten types of particles are randomly generated using the method proposed by Jiang et al. [79], which has been implemented in the PFC2D [78], a commercial DEM software. The

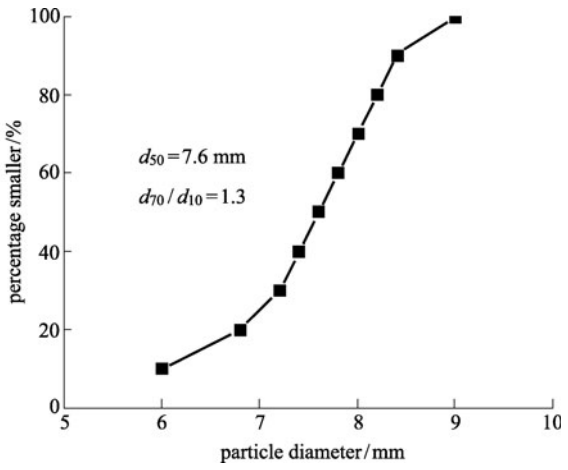

Fig. 2 Distribution of grain sizes in DEM analyses

width and height of the numerical specimens are 800 mm and 1600 mm, respectively. The planar void ratio of the samples is 0.20 before the biaxial tests start, which is representative of a dense granular material. The total number of sand particles in a sample is 24000. Fewer particles, 6000 were used in some preliminary simulations, and there was no significant difference between them in the macro mechanical response. However, we find that this latter number is too small to give rise to accurate information on shear bands, such as shear band width, strain, and rotation fields in the shear bands. In contrast, the 24000-particle specimen in this paper is large enough to obtain reliable information on shear bands, which will be introduced later in detail. This can be regarded as another feature in this study, since previous DEM analyses of strain localization [72–75] in granulates employed too small number of particles lying within the shear band to draw conclusions on the strain, stress, and particle rotating fields outside and within shear bands.

In order to investigate the strain localization of the idealized sand, the membrane boundary widely used in geo-laboratory was employed and simulated with a flexible side boundary consisting of bonded particles, as originally proposed in Refs. [72,80]. The stress-controlled flexible boundary is implemented in the PFC2D using the method that has been also used recently by Wang et al. [65,67]. As already demonstrated in Refs. [72,80] and further confirmed in our preliminary simulations, the employment of flexible membrane boundaries allows DEM specimens to capture deformation characteristics of shear bands in biaxial tests. The input parameters for the grains and membrane particles are provided in Table 1. The top and bottom boundaries are simulated with rigid walls having the same normal and tangential contact stiffness as the sand

Table 1 Sample size and material parameters used in the DEM analyses

samples	parameters	value
size	width of sample /mm	800
	height of sample /mm	1600
	initial void ratio	0.2
sand particles	total number in sample	24000
	density/(kg·m^{-3})	2600
	diameter/mm	gradation in Fig. 2
	normal contact stiffness for test/(N·m^{-1})	7.5×10^{7}
	tangential contact stiffness for test/(N·m^{-1})	5.0×10^{7}
	interparticle coefficient of friction for test	0.5
	coefficient of friction between wall and particle	0.0
	normal contact stiffness for specimen generation/(N·m^{-1})	1.5×10^{10}
	tangential contact stiffness for specimen generation/(N·m^{-1})	1.0×10^{10}
	interparticle coefficient of friction for specimen generation	1.0
	normal contact stiffness between sand and membrane particles/(N·m^{-1})	3.75×10^{6}
	local damping coefficient	0.5
membrane particles	diameter/mm	2.0
	density/(kg·m^{-3})	1000
	normal bond strength in normal direction/N	1.0×10^{100}
	bond strength in tangential direction/N	1.0×10^{100}
	normal contact stiffness/(N·m$^{-1)}$	3.75×10^{6}
	tangential contact stiffness/(N·m^{-1})	2.5×10^{6}

particles. In addition, the coefficient of friction between walls and particles was set to zero to reproduce ideal experimental conditions.

The multilayer under-compaction method proposed by Jiang et al. [79] was implemented in the PFC2D and used to generate the samples in the study. The details on the generation procedure were introduced in Ref. [79]. In this paper, five horizontal layers were used in the specimen generation with each layer containing 4800 particles randomly distributed in a rectangular area 800 mm wide and 437 mm high. Particles were compacted to the target planar void ratio $e_p = 0.20$ by moving downward the top rigid wall at a constant speed of 5.0 m/s with the lateral and bottom walls being fixed. The coefficient of inter-particle friction used during the generation process was $\Phi_\mu = 0.20$, while the wall-particle contacts were set to be frictionless. The under-compaction criterion was satisfied by compacting each layer of particles to its planar void ratio $e_{p1} = 0.224$, $e_{p(1+2)} = 0.221$, $e_{p(1+2+3)} = 0.218$, $e_{p(1+2+3+4)} = 0.212$, and $e_{p(1+2+3+4+5)} = 0.20$, respectively.

After the generation of the samples, the interparticle coefficient of friction was set to 0.5. The samples were then consolidated one-dimensionally under a small vertical pressure of 12.5 kPa with the side walls fixed. In this stage, contacts between particles were found to distribute uniformly in the samples. Then, the samples were subjected to an isotropic constant confining pressure, while two side walls were replaced with membrane particles to simulate the flexible rubber membranes. This corresponds to the consolidation stage in geo-laboratory. Finally, the samples were vertically compressed with the top wall moving downward and the bottom wall moving upward at a constant speed, while the lateral pressure on the specimen remained unchanged on the membrane particles. The compression rate was 5.0% per minute in terms of axial strain rate in all the simulations. This low rate assures that quasi-static condition is always satisfied, the pressure measured on the top and bottom walls is nearly identical to each other during the compression test. and the stress field is uniform within the sample until the occurrence of shear bands.

The main reason for choosing a material of void ratio 0.20 to investigate the strain localization of granular material is that our preliminary study shows that shear band may not necessarily occur in the material of different void ratios. Figure 3 presents the deformation patterns of specimens at failure state with their initial void ratio being 0.25 and 0.20, respectively. Figure 3 shows that shear band does not occur in the specimen with the initial void ratio 0.25 from the viewpoint of naked eye, which corresponds to a loose granular material but occurs in the specimen of initial void ratio 0.20.

A series of biaxial compression tests was performed on the material of void ratio 0.20 under different confining pressures, i.e., 50, 100, 200, and 400 kPa, first to obtain the strength envelope of the material. A complete numerical test was then carried on the material under confining pressure 100 kPa with focus on the relationship between its mechanical behavior and strain localization mechanism. We shall introduce the DEM numerical results in the next sections.

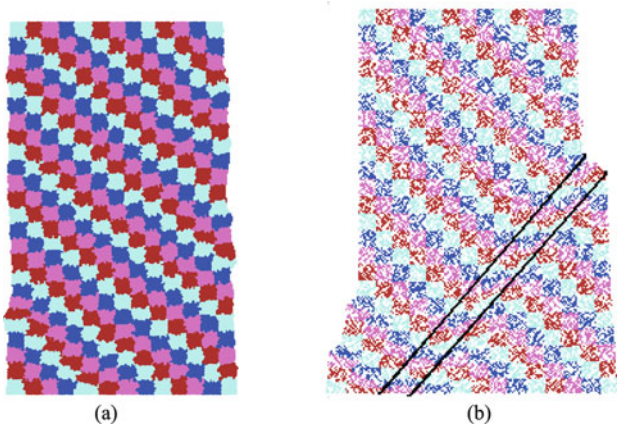

Fig. 3 Deformation patterns at failure of specimens with different initial void ratio. (a) 0.25; (b) 0.20

3 Mechanical behavior of the DEM sample

3.1 Stress-strain and volumetric responses

In order to describe the macroscopic mechanical responses of the sample, the two-dimensional invariant variables were employed, i.e., mean effective stress $p = (\sigma_1 + \sigma_3)/2$, deviatoric stress $q = (\sigma_1 - \sigma_3)/2$, and volumetric strain $\varepsilon_v = \varepsilon_1 + \varepsilon_3$, where σ_1 (ε_1) and σ_3 (ε_3) represent the major and minor principal stress (strain), respectively.

Figure 4 provides the deviatoric stress-axial strain and the volumetric strain-axial strain relationships measured from the whole specimen under confining pressure 100 kPa, in which strain localization occurs. Figure 4 shows that the deviatoric stress increases nonlinearly with the increasing of axial strain at first, then decreases with the axial strain after it reaches its peak value, which is named "strain-softening" in soil mechanics, and finally arrives at a constant residual value. In contrast, the volumetric strain increases (corresponding to compression) at first, then decreases (corresponding to dilation) with the increasing of axial strain, and finally arrives at a constant value. These phenomena are in agreement with the experimental observation on dense sands in Refs. [23–27]. In addition, let points A and A' in Fig. 4 represent the initiation of minishear bands (to be introduced in detail in Fig. 8) and the phase-change point, i.e., a state from which compression turns into dilation. Figure 4 shows that point A coincides with point A', where the axial strain is 0.37%. Note that a state of soils where volumetric strain remains

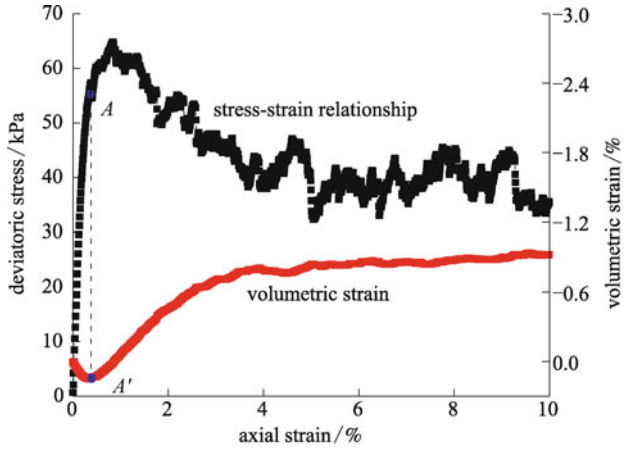

Fig. 4 Stress-strain relationship of the whole specimen in which strain localization occurs

unchanged under a constant deviatoric stress is named the critical state in critical soil mechanics [81].

3.2 Stress path and failure envelopes

Figure 5 provides the stress path the specimen experiences during biaxial compression test, and the predicted envelopes of the peak and residual strengths obtained numerically from the idealized sand. In the figure, the peak (residual) internal frictional angle φ_p (φ_r) is 21.5° (14°). Note that the internal friction angle of real granular materials is usually between 30° and 40°, which is larger than the predicted value. A number of researchers have employed elliptical or other shaped particles in DEM analyses to inhibit particle rotation in order to increase and hence produce more realistic strength values [53, 82–85]. Clustering of the discs [84] and angular grains [85] are efficient to increase the strength. In addition, the predicted value can be increased to a realistic value even for circular discs if the rolling resistance due to grain shape or particle roughness is taken into account [86,87].

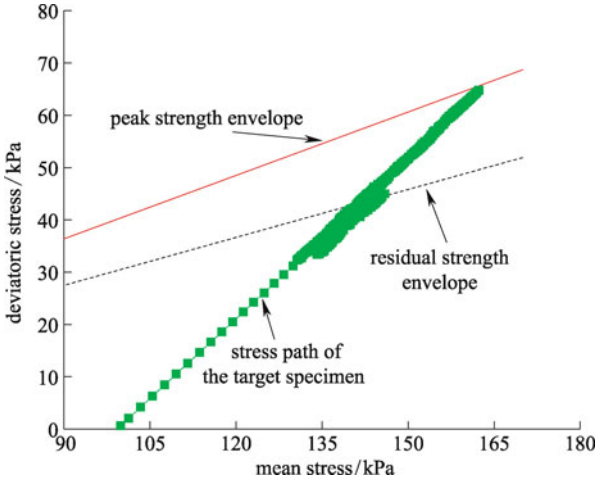

Fig. 5 Stress path that the whole specimen experiences in biaxial compression test

Figure 5 shows that the deviatoric stress increases linearly with the increasing of mean stress up to the peak strength envelope. It then decreases linearly with the mean stress to a state swaying slightly about the residual strength envelope. The numerical results are in agreement with the experimental data obtained from fully drained compression tests on sands, confirming that the numerical test is a fully drained test as planned.

4 Strain localization in the DEM specimen

In this section, the DEM sample will be further examined numerically with regard to strain localization. Based on the stress-strain and volumetric responses of the sample, which is introduced in Fig. 3, the main features of strain localization will be described at five different axial strains: 1) 0.37%, 2) 0.8%, 3) 3.3%, 4) 6%, and 5) 10%. 0.37% is the axial strain where mini-shear bands start to form and where compression turns into dilation. 0.8% corresponds to the peak deviatoric stress, and 3.3% corresponds to the point where the volumetric strain or deviatoric stress starts to become nearly constant. 6% represents a state of strain localization, and 10% is where the test was stopped.

4.1 Deformed specimens

In order to describe clearly deformation pattern of specimen during biaxial compression test, we painted the initial specimen into grids with four different colors before the test started, which was probably the method first employed in DEM analyses by Jiang et al. [68–70]. These painted grids are observed and output to reflect the deformation patterns of the specimen in analogous to the FEA at the abovementioned different axial strains. Each grid of particles is painted with a specific color, and this color remains intact during the test. As shown in Fig. 3, the specimen is painted into 325 quadrilateral grids of four "nodes", which are similar to quadrilateral elements commonly used in FEA. Each grid has an initial width and height close to $8.1d_{50}$ and $8.4d_{50}$, respectively; and this is composed of about 74 particles. The grid size is chosen by considering that 1) it should be small enough to capture the high gradients of variables in the soil about shear band; and 2) it should be large enough to represent a 'continuum element' from the viewpoint of micro and macro-mechanics.

Figure 6 provides the deformation patterns of the DEM sample observed at those different axial strains. Figures 6(a) and (b) show that the strain field is nearly homogeneous in the whole specimen with the naked eye until the specimen arrives at its peak deviatoric stress. Figure 6(c) shows that inhomogeneous deformation is significant enough to be told with the naked eye when the

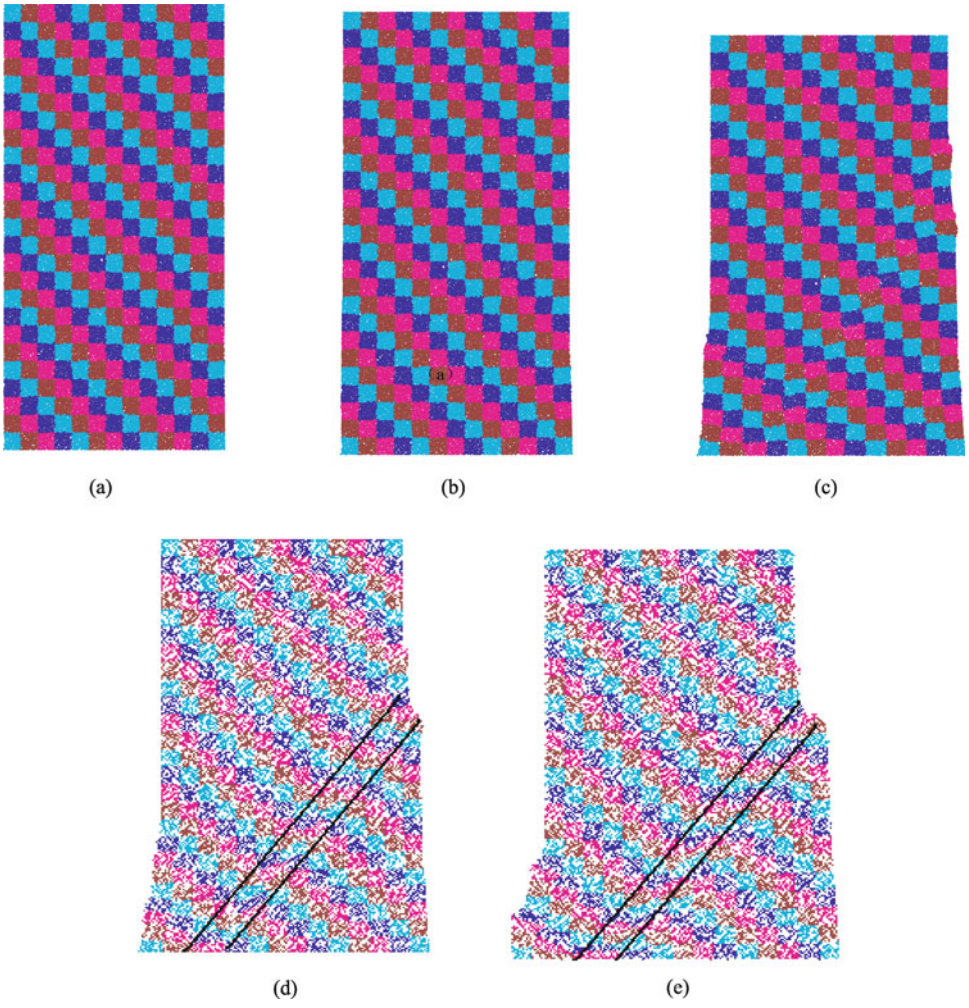

Fig. 6 Deformation patterns of the specimen at different axial strain (initial void ratio: 0.20; cell pressure: 100 kPa). (a) 0.37%; (b) 0.8%; (c) 3.3%; (d) 6%; (e) 10%

specimen arrives at its residual deviatoric stress, while Figs. 6(d) and (e) show that the shear band is more pronounced at the critical state with the increasing of axial strain. In the light of the fact that several mini-shear bands or small shear bands occur before its peak deviatoric stress (to be introduced in Figs. 8(a) and (b)), these results are in agreement with the experimental observations that shear bands are formed progressively in laboratory from the invisible to the visible state with the naked eye [22–30].

4.2 Stress fields

In order to describe the stress state within the sample, particularly during the formation of shear bands, we shall provide the average stress state within a discrete assembly of disks by considering a suitable number of particles within a representative volume and calculating an equivalent stress tensor from the values of contact orientations and forces [51,78]. In this paper, a simplified method implemented in the power factor correction (PFC) code was used to obtain the averaged stress tensor over a circle of particles in the two-dimensional analyses. Our trial simulations show that the accuracy of stresses obtained depends on the radius of the circle for a given grain size distribution. If the circle radius is large enough, e.g., 10–12 times the average particle radius in this paper, the obtained stress value becomes independent of the circle radius, and moreover, the stresses measured in two neighbor circles change in a smooth way.

Figure 7 provides the average stress fields in the expression of principal stress vectors obtained at various stages of loading in the DEM sample. Figures 7 (a) and (b) show that the stress field remains homogeneously distributed and that the direction of the major principle stresses is vertical almost everywhere until the peak deviatoric stress is reached. Figures 7(c)–(e) show that when the deviatoric stress reaches its residual point and the specimen reaches its critical state, the direction of the major principal stresses rotates gradually inside the shear band with their inclination slightly away from the shear

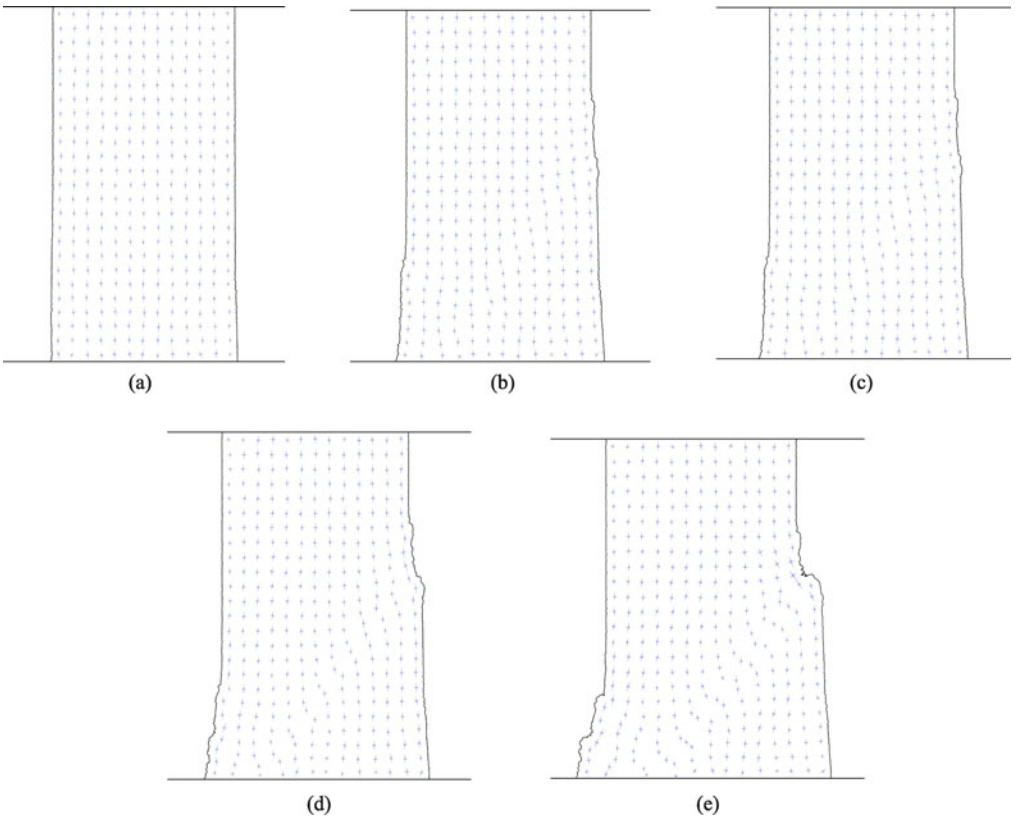

Fig. 7 Distributions of principal stress vectors in the specimen at different axial strain (initial void ratio: 0.20; cell pressure: 100 kPa). (a) 0.37%; (b) 0.8%; (c) 3.3%; (d) 6%; (e) 10%

band but not eventually perpendicular to the shear band. However, the major principal stress vectors are still in a vertical direction in the area away from the shear band.

4.3 Velocity fields

In order to describe the strain fields on the specimen in association with the formation of shear bands, we shall output visually velocity vectors of all particles in black color but with different darkness at the abovementioned axial strains. The quasi-static velocity of each particle is computed by its position change of particle centre. If the maximum velocity V_{max} is measured, each velocity vector is painted with different darkness based on its value. The darkest one represents V_{max}, and the lightest for V_{min}.

Figure 8 provides the distributions of particle velocity vectors in the specimen at different axial strains. Figure 8(a) shows that the velocity field starts to become inhomogeneous at axial strain of 0.37%, showing several mini-shear bands. Such inhomogeneity becomes more significant, and several conjugate small shear bands appear when the peak deviatoric stress is reached, as demonstrated in Fig. 8(b). Figures 8(c)–(d) show that when the specimen arrives at its residual stress and the critical state, these conjugate small shear bands turn into an obvious shear band indicative of shear strain localization. However, Fig. 8(e) shows that when axial strain is 10%, the specimen seems not to be featured with the shear band. Instead, the specimen appears to be composed of two bodies moving in different direction. This observation does not capture the instinct nature of the deformation at this stage. In fact, since the top and bottom walls are assumed to be frictionless in the numerical simulation, the whole specimen moves horizontally in a significant way at this stage, which makes the velocity vectors conceal the feature of shear band. By analyzing the results shown in Figs. 6 and 7 in Sections 4.1 and 4.2 or in Figs. 8 and 9, one can find that strain localization does occur at this stage of axial strain 10%. Hence, the results in Fig. 8 are also in agreement with the experimental observation on formation of shear bands in granulates that several parallel mini-bands are generally formed at first, then turn into several conjugate small shear bands, and finally into an obvious shear band in the specimen [22–30].

4.4 Void ratio distributions

Figure 9 presents distributions of void ratio in the DEM sample obtained at different axial strains. Figures 9(a) and (b) show that the void ratio is neither perfectly homogeneously distributed nor concentrated in a narrow zone before the peak deviatoric stress is reached. In

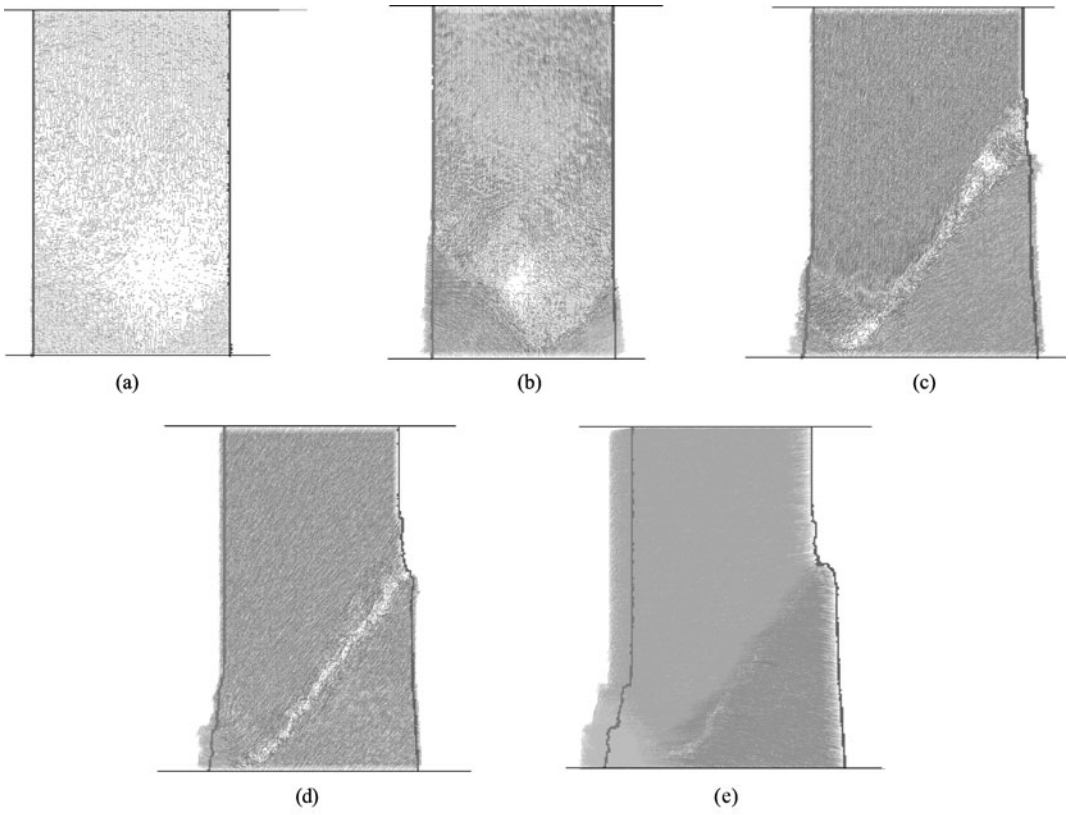

Fig. 8 Distributions of particle velocity vectors in the specimen at different axial strain (initial void ratio: 0.20; cell pressure: 100 kPa). (a) 0.37%; (b) 0.8%; (c) 3.3%; (d) 6%; (e) 10%

contrast, Figs. 9(c)–(e) show that the void ratio becomes larger and larger (i.e., dilation) in a narrow zone, indicating the volumetric strain localization, as the axial strain increases when the specimen is in its critical state. By comparing Figs. 9(c)–(e) with Figs. 8(c)–(e), we find that the volumetric and shear strain localizations occur in the same zone. In addition, Figs. 8(c)–(e) show that the void ratio outside the shear band changes slightly during the test, which indicates that the volumetric dilation of the whole sample comes nearly from the dilation in the shear band. This observation is in agreement with that observed in sands in geo-laboratories [22–30].

It may be interesting to compare the distributions of void ratio in this paper with the results introduced in Ref. [72], which comes from DEM biaxial tests on sand samples using flexible boundaries as well. In Ref. [72], Bardet et al. found that the distribution of void ratio is not helpful in identifying shear bands and therefore concluded that "in two-dimensional materials, the volumetric strain calculated form e or G is inappropriate to detect shear bands." However, they acknowledged that "this observation disagrees with the radiographic measurements of shear bands on real sands in the geo-laboratory." However, our simulations show that strain localization does occur in the granular DEM sample in terms of shear and volumetric strains, and stress field.

4.5 Distributions of averaged pure rotation rate (APR)

It has been recently proven that the energy dissipation between sand particles is related to their relative sliding displacement that can be further expressed in terms of the sliding rotation rate [76,77]. This sliding rotation rate consists of two parts, with one part related to the transmission of particles and the other part to the rotation and size of the particles. The second part named as the pure rotation rate θ^{p} [76,77] can be expressed by

$$\theta^{\mathrm{p}} = \frac{1}{r}(r_1\theta_1 + r_2\theta_2), \tag{1}$$

where r_1 and r_2 are the radius, while θ_1 and θ_2 are the rotation rate of the two particles in contact, respectively. r is the common radius of the two particles in contact defined by

$$r = \frac{2r_1r_2}{r_1 + r_2}. \tag{2}$$

In light of an assembly of sand particles, the averaged pure rotation rate ω (hereafter referred to as APR for short) can be expressed by [76,77]

$$\omega = \frac{1}{N}\sum_{k=1}^{N}\theta^{\mathrm{p}} = \frac{1}{N}\sum_{k=1}^{N}\left[\frac{1}{r^k}\left(\theta_1^k r_1^k + \theta_2^k r_2^k\right)\right], \tag{3}$$

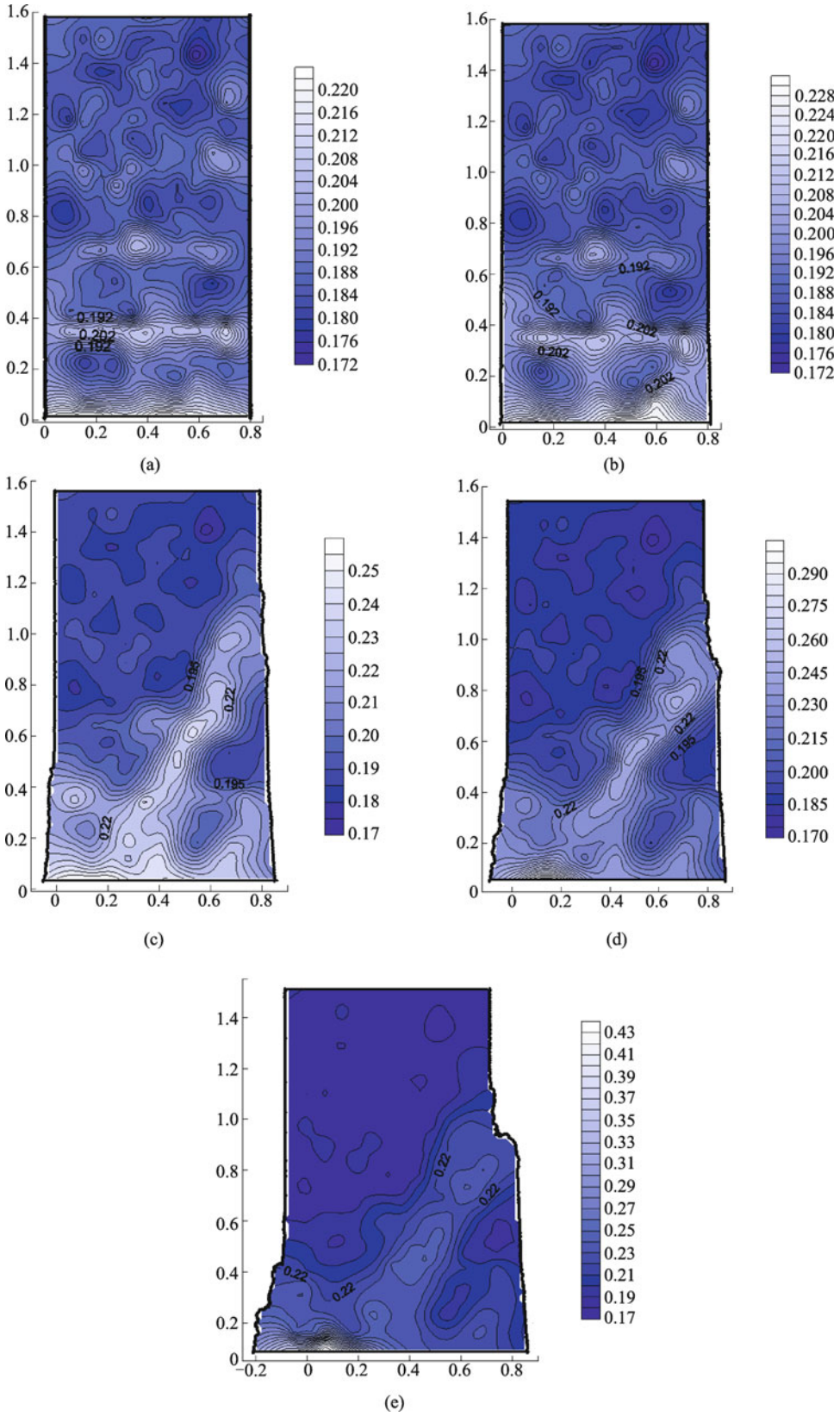

Fig. 9 Distributions of void ratio in the specimen at different axial strain (initial void ratio: 0.20; cell pressure: 100 kPa). (a) 0.37%; (b) 0.8%; (c) 3.3%; (d) 6%; (e) 10%

where N is the total number of the contacts, and r^k is the common radius for the two particles at the kth contact, which can be calculated from Eq. (2). APR is a new variable linking the macro- and micromechanics of sand, which does not exist in classical continuum mechanics. It can be used to constitute other variables that establish the framework of nonclassical continuum mechanics for granulates and have been confirmed to be the right angular velocity sought for decades in the double-shear kinematic models for granulates [58,76,77].

Figure 10 provides APR distributions obtained from the DEM sample at different axial strains mentioned above. In the figure, each APR is obtained from a measurement circle of hundreds of particles. A suitable radius of measurement circle for APR is also chosen to be 10–12 times the average particle radius. Figures 10(a) and (b) show that APR is neither zero in the whole sample nor concentrated in a narrow zone until the peak deviatoric stress is reached. However, Figs. 10(c)–(e) show that the value of APR becomes larger and larger within a narrow zone, which coincides with the shear band introduced in Figs. 6–9, when the specimen arrives at its critical state. In addition, the APR is almost zero and changes slightly outside the shear bands during the test. This observation and those in Figs. 6–9 demonstrate that strain localization in the granular DEM sample is featured not only by deformation pattern, strain and stress fields, and void ratio distribution but also by APR distribution.

4.6 Contact force chains

Figure 11 presents the contact force chains observed in the DEM specimen at the different axial strains, in which the line thickness represents the magnitude of contact forces. Figures 11(a) and (b) show that, as already observed by many other researchers, the distribution of force chains exhibits a webbed pattern with thick chains distributed mostly in the vertical direction in the whole specimen until the peak deviatoric stress is reached. Then, some thicker and column-shaped chains develop progressively with increasing of axial strain in the specimen, as illustrated in Figs. 11(c)–(e). In addition, Figs. 11(c)–(e) show that the thicker column-shaped force chains within the shear band zone, initially in the vertical direction, rotate gradually away from the shear band inclination but still far from becoming perpendicular to the shear band in the specimen. There is no such experimental evidence on it yet, and it is one of our future works to measure the contact force chains with regard to shear bands in laboratory.

4.7 Thickness and inclination of shear bands

Thickness and inclination of shear bands are two main aspects that cannot be well predicted numerically by FEM so far. Since our study shows that the shear band is featured not only by deformation patterns, strain fields, and void ratio distributions but also by APR distributions, we shall investigate the thickness and inclination of shear band in the material using four evaluation criteria in this subsection in terms of deformation patterns, velocity fields, and void ratio and APR distributions. Table 2 presents the characteristics of the shear band at different axial strains where the specimen is at its critical state. Table 2 shows that 1) different evaluation criterion gives rise to slightly different thickness and inclination of shear band. For example, APR is slightly more localized than void ratio; 2) thickness of the shear band is 10–14 times of the mean particle diameter d_{50} on the average and increases generally with the increasing of axial strain; 3) the inclination of the shear band generally decreases with the increasing of axial strain with its value ranging from 54°–50°.

Thickness observed here is in agreement with the previous study [22–30]. Note that the peak (residual) internal frictional angle $\varphi_p\,(\varphi_r)$ is 21.5° (14°), which corresponds to the state at axial strain of 3.3% (6% and 10%) in Table 2. The inclination of shear band predicted by the Mohr-Coulomb theory is $(45° + \varphi/2)$, which gives rise to 55.7° (52°) when $\varphi_p\,(\varphi_r)$ is used. Hence, the Mohr-Coulomb theory can predict the decreasing of the inclination of the shear band against the increasing of axial strain, provided that both the peak and residual internal frictional angles are used. In addition, the inclination of shear band predicted by the Mohr-Coulomb theory is slightly larger than the measured one.

5 Conclusions

This paper presents an insight into the strain localization of idealized sands by DEM analyses. Multilayer under-compaction was employed to generate specimens of a specific grain-size distribution, which were then investigated under biaxial compression tests. Macroscopic responses, including stress-strain relationships, distributions of stress vectors, void ratio and APR, as well as microscopic responses, are examined. In addition, the thickness and inclination of shear bands are investigated. Based on numerical results obtained from the DEM numerical tests, the main conclusions are as follows:

1) The DEM sample demonstrates strain-softening and shear-dilatant mechanical behavior, which is in agreement with experimental results on dense sands. The initiation of minishear bands coincides with the phase-change point, i.e., a state from which compression turns into dilation in specimen.

2) The stress and strain fields are nearly homogeneous in the whole specimen with the naked eye until the specimen arrives at its peak deviatoric stress, while minishear bands or small shear bands occur in fact. When the specimen arrives at its critical state, these conjugate small shear bands turn into a shear band obvious enough to be told

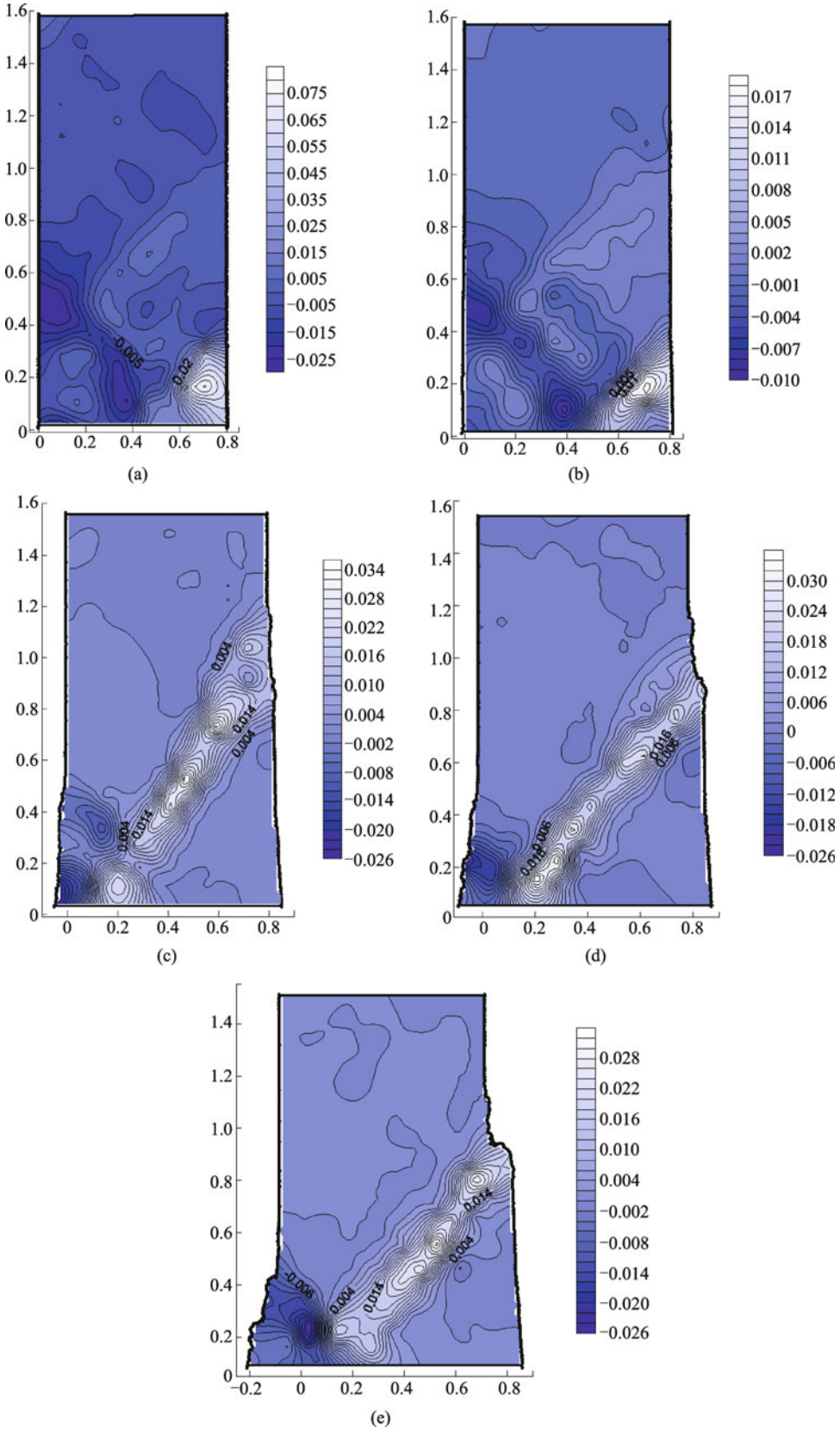

Fig. 10 Distributions of APR in the specimen at different axial strain (initial void ratio: 0.20; cell pressure: 100 kPa). (a) 0.37%; (b) 0.8%; (c) 3.3%; (d) 6%; (e) 10%

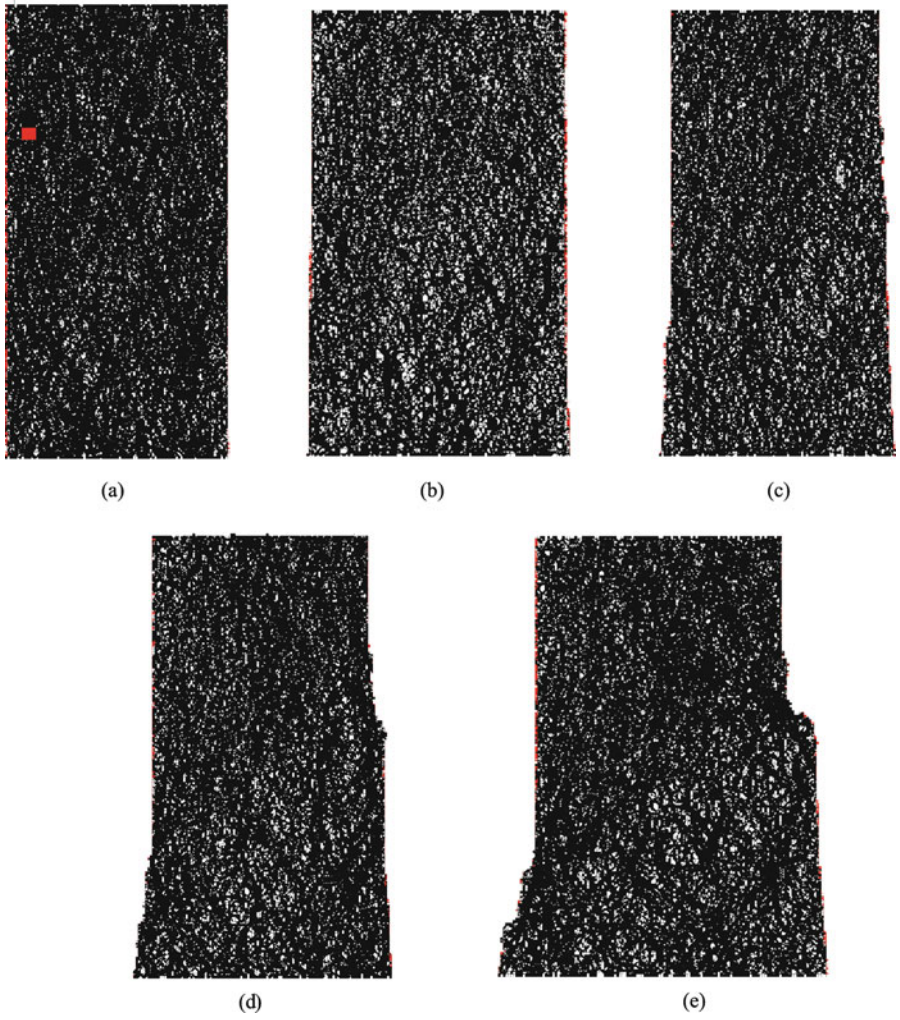

Fig. 11 Force chains in the specimen at different axial strain (initial void ratio: 0.20; cell pressure: 100 kPa). (a) 0.37%; (b) 0.8%; (c) 3.3%; (d) 6%; (e) 10%

Table 2 Characteristics of shear band at different axial strains

characteristics of shear band	evaluation criteria	axial strain		
		3.3%	6%	10%
thickness (d_{50})	deformation pattern	※	14	12
	velocity field	9	10	※
	void ratio distribution	11	15	18
	APR distribution	11	11	12
	averaged thickness	10.3	12.5	14
inclination (degree)	deformation pattern	※	53	49
	velocity field	53	47	※
	void ratio distribution	54	50	52
	APR distribution	54	49	50
	averaged thickness	53.6	49.8	50.3

with the naked eye. In addition, the direction of contact forces and principle stresses rotates gradually inside the shear band with their inclination slightly away from the shear band. Moreover, the void ratio and averaged pure rotation rate (APR) are all localized in the shear band with the values larger inside than outside the shear band.

3) Different evaluation criterion gives rise to slightly different thickness and inclination of shear band.

Thickness of the shear band is 10–14 times of the mean particle diameter d_{50} on the average and increases generally with the increasing of axial strain. The inclination of the shear band generally decreases with the increasing of axial strain with its value ranging from 54°–50°, which can be overall predicted by the Mohr-Coulomb theory.

Acknowledgements This research was financially supported by the National Natural Science Foundation of China (Grant Nos.50679057 and 10972158). These supports are greatly appreciated.

References

1. Jiang Mingjing, Shen Zhujiang. State-of-arts review on strain localisation (shear band) of soils. In: Proceedings of Third Chinese Youth Conference on Geomechanics and Geo-Engineering. Nanjing: Hehai University Publication, 1998, 134–149 (in Chinese)
2. Labuz J, Drescher A. Bifurcations and Instabilities in Geomechanics. Netherlands: Swets & Zeitlinger, 2003
3. Yin J H, Li X S, Yeung A T, Desai C S. In: The International Workshop on Constitutive Modelling Development, Implementation, Evaluation, and Application, Hong Kong. 2007
4. Rudnicki J W, Rice J R. Conditions for localization of deformation in pressure-sensitive dilatant materials. Journal of the Mechanics and Physics of Solids, 1975, 23: 371–394
5. Vardoulakis I. Shear band inclination and shear modulus of sand in biaxial tests. International Journal for Numerical and Analytical Methods in Geomechanics, 1980, 4: 103–119
6. Papamichos E, Vardoulakis I. Shear band formation in sand according to non-coaxial plasticity model. Géotechnique, 1995, 45: 649–661
7. Vardoulakis I, Sulem J. Bifurcation Analysis in Geomechanics. London: Blackie Academic and Professional, 1995
8. Hicher P Y, Wahyudi H, Tessied D. Micro-structural analysis of strain localization in clay. Computers and Geotechnics, 1994, 16: 205–222
9. Jiang M J, Shen Z J. Microscopic analysis of shear band in structured clay. Chinese Journal of Geotechnical Engineering, 1998, 20(2): 102–108
10. Jiang M J, Hongo T, Fukuda M. Pre-failure behaviour of deep-situated Osaka clay. China Ocean Engineering, 1998, 12(4): 453–465
11. Jiang M J, Peng L C, Zhu H H, Lin Y X, Huang L J. Macro- and micro properties of two natural marine clays in China. China Ocean Engineering, 2009, 23(2): 329–344
12. Higo Y, Oka F, Jiang M J, Fujita Y. Effects of transport of pore water and material heterogeneity on strain localization of fluid-saturated gradient-dependent viscoplastic geomaterial. International Journal for Numerical and Analytical Methods in Geomechanics, 2005, 29: 495–523
13. Thomas T. Plastic Flow and Fracture in Solids. Elsevier: Academic Press.1961
14. Rice J R, Rudnicki J W. A note on some features of theory of localization of deformation. International Journal of Solids and Structures, 1980, 16: 597–605
15. Vardoulakis I. Equilibrium bifurcation of granular earth bodies. In: Advances in Analysis of Geotechnical Instabilities. Waterloo: University of Waterloo Press, 1978, 65–119
16. Vardoulakis I. Bifurcation analysis of the triaxial test on sand samples. Acta Mechanica, 1979, 32: 35–54
17. Vardoulakis I. Constitutive properties of dry sand observable in the triaxial test. Acta Mechanica, 1981, 38: 219–239
18. Vardoulakis I. Rigid granular plasticity model and bifurcation in the triaxial test. Acta Mechanica, 1983, 49: 57–79
19. Muhlhaus H B, Vardoulakis I. The thickness of shear bands in granular materials. Geotechnique, 1987, 37: 271–283
20. Vardoulakis I. Shear banding and liquefaction in granular materials on the basis of Cosserat continuum theory. Archive of Applied Mechanics, 1989, 59(2): 106–113
21. Bazant Z P. Softening instability: Part I- Localisation into a planar band. Journal of Applied Mechanics, ASME, 1988, 55: 517–522
22. Arthur J R F, Dunstan T. Rupture layers in granular media. In: Proceedings UTAM Conference on Deformation and Failure of Granular Materials. Rotterdam: Balkema, 1982, 453–459
23. Drescher A, Vardoulakis I. Geometric softening in triaxial tests on granular material. Geotechnique, 1982, 32(4): 291–303
24. Lade P V. Localization effects in triaxial tests on sand. In: Proceedings UTAM Conference on Deformation and Failure of Granular Materials. Rotterdam: Balkema, 1982, 461–471
25. Hettler A, Vardoulakis I. Behaviour of dry sand tested in a large triaxial apparatus. Geotechnique, 1984, 34(2): 183–198
26. Han C. Localisation of deformation in sand. Dissertation for the Doctoral Degree. University of Minnesota, 1991
27. Han C, Drescher A. Shear bands in biaxial tests on dry coarse sand. Soils and Foundations, 1993, 33(1): 118–132
28. Otani J, Mukunoki T, Obara Y. Characterization of Failure and Density Distribution in Soils Using X-Ray CT Scanner. In Proceedings of China-Japan Joint Symposium on Resent Development of Theory & Practice in Geotechnology. Shanghai, 1997, 45–50
29. Nemat-Nasser S, Okada N. Radiographic and microscopic observation of shear bands in granular materials. Geotechnique, 2001, 51 (9): 753–765
30. Harris W W, Viggiani G, Mooney M A, Finno R J. Use of stereophotogrammetry to analyze the development of shear bands in sand. Geotechnical Testing Journal, ASTM, 1995, 18(4): 405–420
31. White D J, Take W A, Bolton M D. Soil deformation measurement using particle image velocimetry (PIV) and photogrammetry. Geotechnique, 2003, 53(7): 619–631
32. Bazant Z P, Kim S S. Plastic fracturing theory for concrete. Mechanical Engineering, ASCE, 1979, 105: 467–478
33. Frantziskonis G, Desai C S. Constitutive model with strain softening. International Journal of Solids and Structures, 1987, 23 (6): 733–750
34. Oritz M, Leroy Y, Needleman A. A finite element method for localised failure analysis. Computer Methods in Applied Mechanics and Engineering, 1987, 61: 189–214
35. Pietruszczak S, Niu X. On the description of localised deformation. International Journal for Numerical and Analytical Methods in

Geomechanics, 1993, 17: 791–805
36. Hoeg K. Finite element analysis of strain-softening clay. Journal of the Soil Mechanics and Foundations, ASCE, 1972, 98(SMI): 43–58
37. Lo K Y, Lee C F. Stress analysis and slope stability in strain-softening materials. Geotechnique, 1973, 23(1): 1–11
38. Yatomi C, Yashima A, Izuka A, Samo I. General theory of shear bands formation by a non-coaxial cam-clay model. Soils and Foundations, 1989, 29(3): 41–53
39. Yatomi C, Yashima A, Izuka A, Samo I. Shear bands formation numerically simulated by a non-coaxial cam-clay model. Soils and Foundations, 1989, 29(4): 1–3
40. Shuttle D A, Smith I M. Localization in the presence of excess pore water pressure. Computers and Geotechnics, 1990, 8: 87–99
41. Pijaudier-Cabot G., Bazant A P. Nonlocal damage theory. Journal of Engineering Mechanics, ASCE, 1987,113: 1512–1533
42. Bazant A P, Pijaudier-Cabot G, Non-local continuum damage, localisation instability and convergence. Journal of Applied Mechanics, 1988, 55: 287–293
43. Bazant A P, Lin F B. Non-local yield limit degradation. International Journal for Numerical Methods in Engineering, 1988, 26: 1805–1823
44. de Borst R, Muhlhous H B. Gradient dependent plasticity formulation and algorithmic aspects. International Journal for Numerical Methods in Engineering, 1992, 35: 521–539
45. de Borst R. Simulation of strain localization: a reappraisal of the Cosserat continuum. Engineering Computations, 1991, 8: 317–332
46. de Borst R. A generalization of J_2 -flow theory for polar continua. Computer Methods in Applied Mechanics and Engineering, 1993, 103: 347–362
47. Steinmann P. Theory and numerics of ductile micropolar elasto-plastic damage. International Journal for Numerical Methods in Engineering, 1995, 38: 583–606
48. Tejchman J, Bauer E. Effect of cyclic shearing on shear localisation in granular bodies. Granular Matter, 2004, 5: 201–212
49. Tejchman J. Influence of a characteristic length on shear zone formation in hypoplasticity with different enhancements. Computers and Geotechnics, 2004, 31(8): 595–611
50. Tejchman J, Niemunis A. FE-studies on shear localization in an anisotropic micro-polar hypoplastic granular material. Granular Matter, 2006, 8: 205–220
51. Cundall P A, Strack O D L. Discrete numerical model for granular assemblies. Geotechnique, 1979, 29: 47–65
52. Ting J M, Corkum B T, Kauffman C R, Greco C. Discrete numerical model for soil mechanics. Journal of Geotechnical and Geoenvironmental Engineering, ASCE, 1989, 115(3): 379–398
53. Rothenburg L, Bathurst R J. Micromechanical features of granular assemblies with planar elliptical particles. Geotechnique, 1992, 42 (1): 79–95
54. Bardet J P. Observations on the effects of particle rotations on the failure of idealized granular materials. Mechanics of Materials, 1994, 18: 159–182
55. Kuhn M R. Structured deformation in granular materials. Mechanics of Materials, 1999, 31(6): 407–429
56. Ng T T. Fabric evolution of ellipsoidal arrays with different particle shapes. Journal of Engineering Mechanics, 2001, 127(10): 994–999
57. Thornton C. Numerical simulation of deviatoric shear deformation of granular media. Geotechnique, 2000, 50(1): 43–53
58. Jiang M J, Harris D, Yu H S. Kinematic models for non-coaxial granular materials, Part II: Evaluation. International Journal for Numerical and Analytical Methods in Geomechanics, 2005, 29(7): 663–689
59. Kuhn M R, Mitchell J K. New perspectives on soil creep. Journal of Geotechnical and Geoenvironmental Engineering, 1993, 119(3): 507–524
60. Jiang M J, Leroueil S, Konrad J M. Insight into shear strength functions of unsaturated granulates by DEM analyses. Computer & Geotech, 2004, 31(6): 473–489
61. Jiang M J, Lerouil S, Konrad J M. Yielding of microstructured geomaterial by DEM analysis. Journal of Engineering Mechanics, ASCE, 2005, 131(11): 1209–1213
62. Jiang M J, Yu H S. Leroueil S. A simple and efficient approach to capturing bonding effect in naturally-microstructured sands by discrete element method. International Journal for Numerical Methods in Engineering, 2007, 69: 1158–1193
63. Utili S, Nova R. DEM analysis of bonded granular geomaterials. International Journal for Numerical and Analytical Methods in Geomechanics, 2008, 32(17): 1997–2031
64. Delenne J Y, El Youssoufi M S, Cherblanc F, Beneet J C. Mechanical behaviour and failure of cohesive granular materials. International Journal for Numerical and Analytical Methods in Geomechanics, 2004, 28: 1577–1594
65. Wang Y H, Leung S C. A particulate scale investigation of cemented sand behaviour. Canadian Geotechnical Journal, 2008, 45: 29–44
66. Jiang M J, Yu H S, Harris D. Bond rolling resistance and its effect on yielding of bonded granulates by DEM analyses. International Journal for Numerical and Analytical Methods in Geomechanics, 2006, 30(7): 723–761
67. Wang Y H, Leung S C. Characterization of cemented sand by experimental and numerical investigations. Journal of Geotechnical and Geoenvironmental Engineering, ASCE, 2008, 134(7): 992–1004
68. Jiang M J, Yu H S, Harris D. Discrete element modelling of deep penetration in granular soils. Journal for Numerical and Analytical Methods in Geomechanics, 2006, 30(4): 335–361
69. Jiang M J, Zhu H H, Harris D. Classical and nonclassical kinematic fields of two-dimensional penetration tests on granular ground by discrete element method analyses. Granular Matter, 2008, 10: 439–455
70. Jiang M J, Harris D, Zhu H H. Future continuum models for granular materials in penetration analyses. Granular Matter, 2007, 9: 97–108
71. Jiang M J, Yu H S. An interpretation of the internal length in Chang's couple-stress continuum for bonded granulates. Granular Matter, 2007, 9: 431–437
72. Bardet J P, Proubet J. A numerical investigation of the structure of persistent shear bands in granular media. Geotechnique, 1991, 41: 599–613
73. Iwashita K, Oda M. Rolling resistance at contacts in simulation of shear band development by DEM. Journal of Engineering Mechanics, ASCE, 1998, 124: 285–292
74. Iwashita K, Oda M. Micro-deformation mechanism of shear banding process based on modified distinct element. Powder Technology, 2000, 109: 192–205

75. Oda M, Iwashita K. Study on couple stress and shear band development in granular media based on numerical analyses. International Journal of Engineering Science, 2000, 38: 1713–40
76. Jiang M J, Yu H S, Harris D. Kinematic variables bridging discrete and continuum granular mechanics. Mechanics Research Communications, 2006, 33: 651–666
77. Jiang M J, Harris D, Yu H S. Kinematic models for non-coaxial granular materials, Part I: theories. International Journal for Numerical and Analytical Methods in Geomechanics, 2005, 29(7): 643–661
78. Itasca Consulting Group Inc. Particle Flow Code in 2 Dimensions, version 3.1. Minnesota, USA, 2004
79. Jiang M J, Konrad J M, Leroueil S. An efficient technique for generating homogeneous specimens for DEM studies. Computers and Geotechnics, 2003, 30(7): 579–597
80. Kuhn M R. A flexible boundary for three-dimensional DEM particle assemblies. Engineering Computations, 1995, 12: 175–183
81. Schofield A N, Wroth C P. Critical State Soil Mechanics. London: McGraw–Hill, 1968
82. Ting J M, Meechum L R, Rowell J D. Effect of particle shape on the strength and deformation mechanism of ellipse-shaped granular assemblages. Computer Engineering, 1995, 12: 99–108
83. Sawada S, Pradhan T B S. Analysis of anisotropy and particle shape by distinct element method. In: Siriwardane H J, Zaman M M, eds. Computer Methods and Advancements in Geomechanics. Rotterdam: Balkema; 1994, 665–670
84. Thomas P A, Bray J D. Capturing nonspherical shape of granular media with disk clusters, Journal of Geotechnical and Geoenvironmental Engineering ASCE, 1999, 125: 169–178
85. Ullidtz P. Modelling of granular materials using the discrete element method. In: Proceedings of 8th International Conference on Asphalt Pavements, University of Washington, 1997, 757–769
86. Jiang M J, Yu H S, Harris D. A novel discrete model for granular material incorporating rolling resistance. Computers and Geotechnics, 2005, 32(5): 340–357
87. Jiang M J, Leroueil S, Zhu H H, Yu H S, Konrad J M. Two-dimensional discrete element theory for rough particles. International Journal of Geomechanics, ASCE, 2009, 9(1): 20–33